Unified analysis of ensemble and single-complex optical spectral data from light-harvesting complex-2 chromoproteins for gaining deeper insight into bacterial photosynthesis

Mihkel Pajusalu,[1] Ralf Kunz,[2] Margus Rätsep,[1] Kõu Timpmann,[1] Jürgen Köhler,[2] and Arvi Freiberg[1,3,*]

[1]*Institute of Physics, University of Tartu, Ravila 14c, 50411 Tartu, Estonia*

[2]*Experimental Physics IV and Bayreuth Institute for Macromolecular Research, University of Bayreuth, 95440 Bayreuth, Germany*

[3]*Institute of Molecular and Cell Biology, University of Tartu, Riia 23, 51010 Tartu, Estonia*

(Received 29 January 2015; revised manuscript received 30 August 2015; published 9 November 2015)

Bacterial light-harvesting pigment-protein complexes are very efficient at converting photons into excitons and transferring them to reaction centers, where the energy is stored in a chemical form. Optical properties of the complexes are known to change significantly in time and also vary from one complex to another; therefore, a detailed understanding of the variations on the level of single complexes and how they accumulate into effects that can be seen on the macroscopic scale is required. While experimental and theoretical methods exist to study the spectral properties of light-harvesting complexes on both individual complex and bulk ensemble levels, they have been developed largely independently of each other. To fill this gap, we simultaneously analyze experimental low-temperature single-complex and bulk ensemble optical spectra of the light-harvesting complex-2 (LH2) chromoproteins from the photosynthetic bacterium *Rhodopseudomonas acidophila* in order to find a unique theoretical model consistent with both experimental situations. The model, which satisfies most of the observations, combines strong exciton-phonon coupling with significant disorder, characteristic of the proteins. We establish a detailed disorder model that, in addition to containing a C_2-symmetrical modulation of the site energies, distinguishes between static intercomplex and slow conformational intracomplex disorders. The model evaluations also verify that, despite best efforts, the single-LH2-complex measurements performed so far may be biased toward complexes with higher Huang-Rhys factors.

DOI: 10.1103/PhysRevE.92.052709 PACS number(s): 87.15.ag, 87.15.ak, 87.15.M−, 87.15.hp

I. INTRODUCTION

Photosynthetic purple bacteria contain highly symmetrical light-harvesting complexes (also called antenna complexes) that transform photons into excitons and transport the absorbed energy into reaction centers, where conversion into chemical energy occurs [1]. The light-harvesting efficiency of these organisms is significantly enhanced by the excitonic interactions [2,3] present in the antenna complexes, which not only broaden their energy spectrum, but also, by the virtue of suitably building up a ladder of exciton states, allow for ultrafast energy transfer with minimal losses [4,5]. Due to the established strong exciton-phonon interaction, the antenna excitations have been proposed to localize, leading to the formation of exciton polarons and/or self-trapped excitons (STEs) [6–8].

Optical properties of light-harvesting complexes from different species of purple bacteria have usually been studied in large ensembles, but during the past two decades the spectroscopy of single complexes has also become increasingly popular [9–18]. Both the ensemble and single-complex approaches have their advantages and disadvantages. While single-complex spectroscopy allows studying the fluorescence and excitation spectra of an individual antenna complex in great detail, the signal-to-noise ratio of such measurements is rather low. Also, the matrices the complexes are immobilized in may influence the sample properties, as was determined for a plant photosystem I in [19] and for bacterial light-harvesting complex-2 (LH2) complexes in [20]. Measuring large ensembles, on the other hand, usually yields excellent signal-to-noise ratios, but predicting the behavior of individual complexes within the large ensemble is not possible without making difficult to prove assumptions.

This leads to the need to compare the two classes of spectroscopic methods and to investigate if they can be used to reach the same conclusions independently and if the conclusions match the ones reached when both cases are studied simultaneously using a quantum mechanical model. For example, in nature each individual protein complex exists in its own configuration, which constantly changes in time, influenced by both electrical and mechanical disturbances in the local microenvironment of the complex. As a result, each complex acquires a slightly different energy spectrum as well as relaxation dynamics, forming a virtually continuous distribution of properties in the case of ensembles of complexes and ultimately in a functioning cell. However, ensemble and single-molecule spectroscopies might probe this ensemble differently and reach different conclusions due to the limitations of the methods.

To study these effects, we focus on the low-temperature optical spectra of the LH2 complex from *Rhodopseudomonas (Rps.) acidophila*. The complex [1,21] consists of two circular arrangements of bacteriochlorophyll *a* (BChl *a*) chromophores, commonly called the B800 and B850 rings (see Fig. 1). These names refer to the positions of absorption maxima in the near-infrared (at about 800 nm and 850 nm, respectively) spectral range related to the Q_y singlet electronic transitions of BChl *a*. Here we only deal with the photoexcitations in the tightly packed B850 ring because the B800 ring excitations end up in the B850 ring already within about 1 ps [25]. By analyzing the experimental single-complex and ensemble spectra of the B850 excitations in parallel, we have developed a theoretical model (see Sec. II), which is verified in

*Corresponding author: arvi.freiberg@ut.ee

 ©2015 American Physical Society

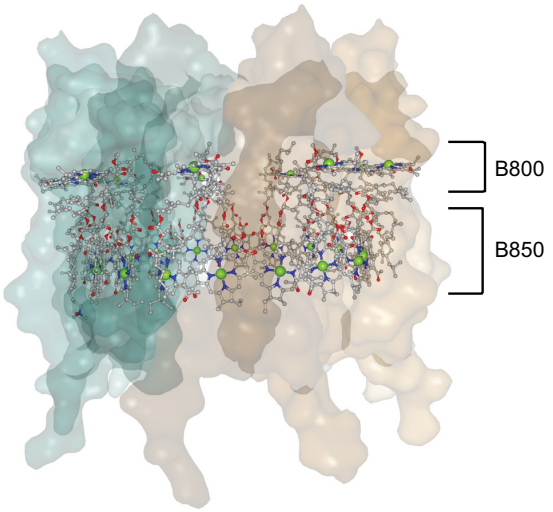

FIG. 1. (Color online) Side view of the LH2 integral membrane antenna complex from *Rhodopseudomonas acidophila* showing the B800 and B850 rings of 9 and 18 BChl *a* chromophores, respectively [22–24]. The imaginary membrane plane is perpendicular to the plane of the figure.

Sec. IV to be representative for both individual-complex and macroscopic ensemble limits.

II. THEORETICAL MODEL

A single B850 ring contains 18 BChl *a* chromophores (in the following referred to as sites), which we index by n and order according to their angles around the symmetry axis of the LH2 complex. Due to the excitonic interaction, each individual antenna complex can be excited into 18 separate excitonic states, numbered from $k = 0$ to $k = 17$, where the state $k = 0$ has the lowest excitation energy and the $k = 17$ state the highest.

With diagonal (energetic) disorder included, the B850 excitonic system could be described by a disordered rigid-lattice Hamiltonian H_0 [26],

$$H_0 = \sum_n \left(\varepsilon_n + \delta\varepsilon_n^{\text{inter}} + \delta\varepsilon_n^{\text{intra}}\right)|n\rangle\langle n| + \sum_{\substack{n,m \\ n\neq m}} t_{nm}|n\rangle\langle m|, \tag{1}$$

where ε_n are the site excitation energies, $\delta\varepsilon_n^{\text{inter}}$ and $\delta\varepsilon_n^{\text{intra}}$ denote, respectively, the intercomplex and intracomplex energetic disorders, and t_{nm} designates the coupling energy between sites n and m. Intercomplex disorder stands for the variations in time-averaged site energies that are different from complex to complex. Intracomplex disorder stands for the variations of the site energies in experimentally measurable time scales within a complex. It should be noted that in Eq. (1), disorder is applied only to the diagonal elements of the coupling matrix. This is mathematically more convenient [4] and has also been verified to produce almost indistinguishable results from the off-diagonal disorder model for the actual range of disorder parameters [27]. See below for more details.

When deformations are allowed in the system, the excitons can localize, leading to a new possible set of excited states. Next we present a theoretical model for describing the B850 excitonic system allowing self-trapping of the excitons [6–8]. The exciton self-trapping process can be modeled by including deformation parameters q_n that modify either the diagonal elements of the coupling matrix, like in the Holstein Hamiltonian [28], or the off-diagonal couplings, like in the case of the Su-Schrieffer-Heeger Hamiltonian [29]. Both variants have been used to describe molecular aggregates in the literature (examples for the former can be found in [30–33] and for the latter in [34–37]). It has also been shown that off-diagonal coupling can in principle be mapped to diagonal coupling [38]. We will continue with the model containing distortions in the interpigment coupling since this model performed slightly better in our tests and also because a similar approach was used in our previous work [4], allowing comparison

$$H = H_0 + c\sum_n q_n(|n\rangle\langle n+1| + |n+1\rangle\langle n|) + cq_{17}(|17\rangle\langle 0| + |0\rangle\langle 17|) + \frac{1}{2}\sum_n q_n^2, \tag{2}$$

where c determines the strength of the coupling of deformations q_n to the off-diagonal couplings (i.e., strength of self-trapping) and the last term on the right-hand side describes the energy associated with the deformations.

Note that we are using the Hamiltonian only to model the eigenstate changes due to self-trapping, which essentially produces a stick spectrum. The exciton-phonon bath interaction leading to phonon sidebands, essential for comparison with the experimental spectra, is later included as dressing of the excitonic states phenomenologically. As we are dealing with a circular (not linear) aggregate, we are using the component $c\,q_{17}(|17\rangle\langle 0| + |0\rangle\langle 17|)$ to include the couplings between the first and the last element of the chain ($n = 0$ and $n = 17$).

For the Hamiltonian (2), the values of distortions q_n are found by using an iterative procedure [39]. The distortions are considered static during the lifetime of the STE. The procedure starts by applying a guess value for the distortions, then the Hamiltonian is diagonalized, and a new set of optimal distortions is calculated from the wave functions using the condition $\partial H/\partial q_n = 0$. The procedure, which is repeated until convergence, yields the eigenenergies of STE states E_k and a matrix consisting of eigenvectors a_{mk} (see [4,6] and references therein for more details):

$$\sum_m \langle n|H|m\rangle a_{mk} = E_k a_{nk}. \tag{3}$$

In the B850 ring, the 18 BChl *a* sites are pairwise coordinated by α- and β-transmembrane protein helices that are arranged into 9 similar heterodimers [21,22,40]. Therefore, even in an ordered state, the site excitation energies may differ from each other and can be written as $\varepsilon_{2n} = \nu + \Delta/2$ and $\varepsilon_{2n+1} = \nu - \Delta/2$ for the chromophores coordinated to α and β helices, respectively. The previously published [6,41–44] values of the average site excitation energy ν vary between 12 160 and 12810 cm^{-1}, while the difference Δ between the α-and β-coordinated site excitation energies varies between 0 and 532 cm^{-1}. The interpigment coupling energies have commonly been calculated from structural data using a simple exciton model in a dipole-dipole approximation [45] or by the means of more sophisticated quantum chemical

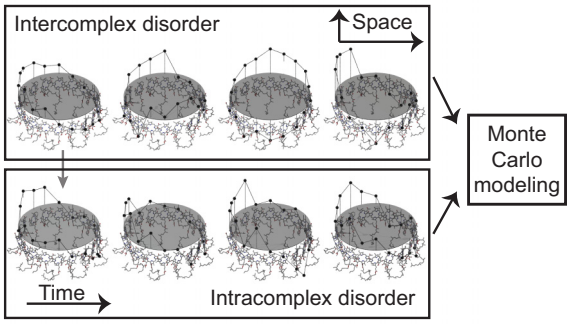

FIG. 2. (Color online) In a low-temperature glassy matrix, each LH2 complex acquires a slightly different configuration due to the spatially varying microenvironment. This is considered to result in the intercomplex disorder. Each and every individual complex occasionally changes its conformation, causing spectral fluctuations within the experimental time frame. These slowly fluctuating spectra are modeled by sampling the intracomplex disorder multiple times for the same complex (here explicitly shown for the leftmost complex in the top panel). The changes in site transition energies within the B850 ring along spatial (top) and temporal (bottom) coordinates are shown by black dots (the lines connecting dots are drawn to guide the eye). Dots on the gray disk plane represent the idealized case of zero energetic disorder.

models [46–48]. The former approach was applied in the present work. The mean structure parameters were taken from [21,45], but were considered loose for fitting in a range of a few percent. The model parameters used are further characterized below.

Like previously [49–51], the diagonal disorder is divided into two parts comprising the intercomplex disorder $\delta\varepsilon_n^{\text{inter}}$ and the intracomplex disorder $\delta\varepsilon_n^{\text{intra}}$. Yet the essence of these terms is more involved, as illustrated in Fig. 2. In the previous models, both types of disorder were taken to be static, whereas here only the intercomplex disorder (resulting from specific microenvironments of individual complexes) is considered as static. The intracomplex disorder, representing slow conformational changes in each and every complex, is considered dynamic. The excitation and/or emission spectra of single complexes, measured in the presently accessible experimental time scale of 1 s and longer, clearly manifest significant changes when repeatedly recorded over time, even at very low temperatures [11,19,52–56]. These relatively slow dynamics should be distinguished from the fast dynamics due to exciton-phonon coupling, which is responsible for the homogenous broadening of the spectra as well as for the exciton self-trapping. These latter processes will be introduced via a phonon spectral density function (SDF), as described further below.

For a particular complex, the dynamical nature of the disorder is simulated by sampling different realizations of the intracomplex site energy disorder. The intracomplex disorder elements $\delta\varepsilon_n^{\text{intra}}$ are sampled from a Gaussian distribution with a standard deviation of σ_{intra}.

The intercomplex disorder (4) comprises two Gaussian site energy distributions (one for $\delta\varepsilon^u$ and another for $\delta\varepsilon_{\text{shift}}$) and a modulation of C_2 symmetry, also known as elliptic distortion. This specific distortion was empirically included because it allows one to reproduce the large splitting of the B850 absorption band, which was observed in single-complex measurements (see [57] and references therein):

$$\begin{aligned}\delta\varepsilon_{2n}^{\text{inter}} &= \delta\varepsilon_{2n}^{u} + \delta\varepsilon_{\text{shift}} + \xi_1 \cos\left(2n\frac{\pi}{9} + \phi_{1\alpha}\right) \\ &\quad + \xi_2 \cos\left(4n\frac{\pi}{9} + \phi_{2\alpha}\right), \\ \delta\varepsilon_{2n+1}^{\text{inter}} &= \delta\varepsilon_{2n+1}^{u} + \delta\varepsilon_{\text{shift}} + \xi_1 \cos\left(2n\frac{\pi}{9} + \phi_{1\beta}\right) \\ &\quad + \xi_2 \cos\left(4n\frac{\pi}{9} + \phi_{2\beta}\right),\end{aligned} \tag{4}$$

where $\delta\varepsilon^u$ is an uncorrelated diagonal disorder, sampled from a Gaussian distribution with a standard deviation σ_{inter} for each individual site in the complex separately; $\delta\varepsilon_{\text{shift}}$ is the energetic shift, sampled once per complex from a Gaussian distribution with a standard deviation of $\sigma_{\text{energetic}}$; ξ_1 and ξ_2 are the modulation strengths of the C_2-symmetry site-energy disorder sampled from Gaussian probability distributions with the respective standard deviations as model parameters; and $\varphi_{1\alpha}$, $\varphi_{2\alpha}$, $\varphi_{1\beta}$, and $\varphi_{2\beta}$ are the random phase parameters sampled from a uniform distribution of angles and no model parameters are associated with them.

The previous, simpler, models of intercomplex disorder included only the $\delta\varepsilon_{\text{shift}}$ term, which simultaneously shifts all the site energies by a given value. The additional terms introduce a dependence on n, thereby modifying the individual exciton state energies and other spectral parameters, such as the Huang-Rhys factors, i.e., the average numbers of phonons involved in the absorption or emission process. The specific realization of the intercomplex disorder is cumulative with the intracomplex disorder, which also means that the same intracomplex disorder would cause different results in final eigenstates if applied to different complexes (with different realizations of intercomplex disorder).

As an example, Fig. 3 shows the site distributions of different components of disorder corresponding to the fitting parameters presented in Table I. Shown is just a single realization of disorder, but the C_2 modulation in general dominates over all other types of disorder.

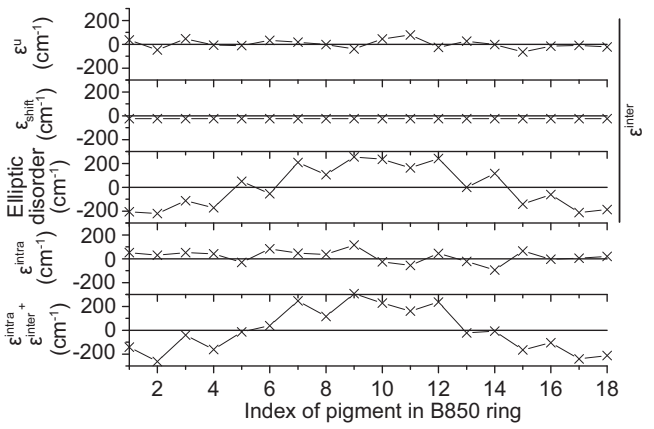

FIG. 3. Example of different components of disorder corresponding to the fitting parameters in Table I.

TABLE I. Model parameters evaluated from the fit of the bulk ensemble spectra.

Parameter	Description	Value
ω_c	Shape parameter of the phonon SDF	24 cm^{-1}
S	Huang-Rhys factor of the site	9.7
$c^2/2$	Parameter describing the strength of self-trapping	55 cm^{-1}
σ_{intra}	Standard deviation of the intracomplex disorder	40 cm^{-1}
σ_{inter}	Standard deviation of the intercomplex disorder	30 cm^{-1}
σ_{E1}	Standard deviation of the strengths of the first mode of elliptic modulation [ξ_1 in Eq. (43)]	190 cm^{-1}
σ_{E2}	Standard deviation of the strengths of the second mode of elliptic modulation [ξ_2 in Eq. (43)]	130 cm^{-1}
$\sigma_{\text{energetic}}$	Standard deviation of the noise applied to all of the site energies of a complex as intercomplex disorder [$\delta\varepsilon_{\text{shift}}$ in Eq. (43)]	20 cm^{-1}
Δ	Difference between the α- and β-coordinated site transition energies	295 cm^{-1}
E	Mean of α- and β-coordinated site transition energies	12290 cm^{-1} (814 nm)
γ	FWHM of the lifetime broadening for the states $k = 1$–17 (broadening of $k = 0$ is ignored) [6,58–60]	80 cm^{-1}

The line shape corresponding to a BChl *a* site (taken to be similar for all sites) is modeled using a phenomenological phonon SDF, which at absolute zero temperature is conveniently defined by just two parameters, the characteristic frequency ω_c and the Huang-Rhys factor S [61],

$$J(\omega \geqslant 0) = \omega \exp\left(-\frac{\omega}{\omega_c}\right)\frac{S}{\omega_c^2}. \tag{5}$$

Here S is considered to be the main parameter determining the strength of the exciton-phonon coupling. The phonon SDF of Eq. (5) lacks the part of the vibrations that are localized on the BChl *a* sites. This is an experimentally well justified simplification, due to the almost complete absence of vibronic structure in the fluorescence spectrum of the B850 ring [62]. Although we have applied more involved SDF forms before [4,63], the use of the simpler shape is warranted by the low signal-to-noise ratio of single-complex measurements.

The homogeneous absorption and emission spectral profiles can be calculated as [64]

$$I(\omega) = \sum_{n=0}^{\infty} \frac{S^n e^{-S}}{n!} J_n(\omega), \tag{6}$$

where $J_n(\omega)$ is the nth convolution of $J(\omega)/S$ with itself. Its $n = 0$ component corresponds to the zero-phonon line (ZPL), while the higher-order components form the phonon sideband (PSB). The actual modeling was done over the exponent of the Fourier transform of the phonon SDF, as described in [65]; this procedure is computationally cheaper yet mathematically equivalent.

The effect of excitonic coupling on the phonon SDF of a given exciton state is accounted for through the participation ratio $p_k = \sum_n |a_{nk}|^4$, which is the inverse of the delocalization length [6,27,66–69]. The effective Huang-Rhys factor for a particular STE state k, S_k, is defined as

$$S_k = S \sum_n |a_{nk}|^4 = S p_k, \tag{7}$$

where S is the site Huang-Rhys factor, corresponding to the case where the exciton is localized on a single BChl *a* site. Thus S_k would be the greatest if the exciton were localized on a single site (delocalization length equal to 1). In the opposite extreme of complete delocalization, which corresponds to an idealized B850 ring with all the sites having similar excitation energy, $S_k = S/18$.

The transition dipole moments of the STE states are evaluated as

$$D_k = \sum_n a_{nk}\mu_n, \tag{8}$$

where μ_n are the transition dipoles of individual BChl *a* chromophores. Applying Eq. (8), the absorption $A(\omega)$ and fluorescence emission $F(\omega)$ spectra corresponding to STEs in the B850 ring were calculated as

$$\begin{aligned} A(\omega) &\propto \sum_k \omega D_k^2 I(\omega - E_k), \\ F(\omega) &\propto \omega^3 D_0^2 I(E_0 - \omega). \end{aligned} \tag{9}$$

The ensemble spectra are found by summing up a large number of individual spectra with the randomly generated realizations of disorder.

In Eqs. (9) the information about the energies and eigenvectors of the STE (3), the scaled Huang-Rhys factors (7), and the spectral profiles (6) as well as the lifetime broadening of the states (see Table I) is implicitly included into the line-shape functions $I(\omega - E_k)$ and $I(E_k - \omega)$. At very low temperatures, such as those employed in the current experiments (1.2 and 4.5 K), the emission stems predominantly from the lowest excited state; therefore, contributions from higher STE states to the fluorescence were neglected when simulating the emission spectra. Hence, in the present model, a single-complex emission spectrum is determined by only three parameters: the excitation energy of the lowest state E_0, which determines the position of the ZPL; the Huang-Rhys factor of the same state S_0, which governs the mean number of phonons involved in the emission process; and the characteristic frequency ω_c.

The bulk ensemble fluorescence excitation anisotropy spectra $r(\omega)$ are calculated as [2,4,5]

$$r(\omega) = \left\langle \frac{3\cos\alpha_k - 1}{5} \right\rangle_k = \frac{F_{||}(\omega) - F_{\perp}(\omega)}{F_{||}(\omega) + 2F_{\perp}(\omega)}, \qquad (10)$$

where $F_{||}(\omega)$ designates the integral emission detected parallel to the polarization of the exciting laser and $F_{\perp}(\omega)$ that detected perpendicular with respect to excitation, ω is the excitation frequency, and α_k is the angle between the transition dipole of the absorbing state k and the lowest-energy emitting state. For comparison with experiment, the calculated spectra were convoluted with the relevant instrumental response functions (IRFs). The lowest state lifetime (>1 ns [7]) causes negligible broadening compared with the IRF. However, lifetime broadening of the higher-energy states may be considerable.

III. EXPERIMENTAL DATA ANALYZED

The above model was developed for a cohesive understanding of the optical spectroscopy of individual LH2 complexes as well as their ensembles. Types of the spectra under consideration include fluorescence and fluorescence excitation for individual complexes and fluorescence, fluorescence excitation, and fluorescence excitation anisotropy for large ensembles of complexes. The sample of choice, for which all these spectra are available, is the LH2 complex from *Rps. acidophila*. Some of the spectra of single complexes and ensembles of the complexes used in this work have been published [70–72]. Single complexes were immobilized in polyvinyl alcohol (PVA) film and studied at 1.2 K. The bulk samples measured at 4.5 K were prepared almost identically by just using a much larger concentration of LH2 complexes. In the context of this paper, the temperature difference applied in single-complex and ensemble measurements is negligible. It has also been shown that embedding antenna complexes from purple bacteria into PVA film yields essentially the same statistical data as reconstitution into a lipid bilayer that mimics a more natural environment [73,74].

For experimental details the reader is referred to Refs. [70–72]. Here we repeat only the most important aspects of the experiments. The time required for measuring a single-complex fluorescence-excitation spectrum by scanning a laser over the Q_y exciton absorption range was 15–20 s and this was repeated for up to 1 h in order to produce the time-averaged excitation spectra presented here (individual scans can be seen in [73]). Individual fluorescence spectra were recorded faster, within 3–10 s, by exciting the sample in the B800 absorption band. A large number of these were averaged to produce a long integration time spectrum. When measuring excitation spectra, the fluorescence was recorded through bandpass filters by using a single photon counting avalanche photodiode [70,72]. In the fluorescence-emission measurements the signal was directed through long-pass filters to suppress the exciting laser and a monochromator toward a CCD camera for detection [70–74]. The complexes were selected for study by exciting the sample with a laser operating at 855 nm and imaging the emission through a set of identical bandpass filters. Spectral characteristics of these filters turn out to play an important role, as will be explained shortly.

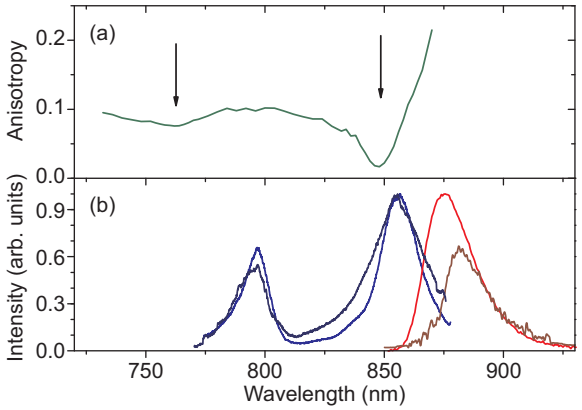

FIG. 4. (Color online) Comparison of the ensemble (a) fluorescence excitation anisotropy and (b) fluorescence excitation (blue) and fluorescence (red) spectra of LH2 complexes from *Rps. acidophila* with the sum of the (b) excitation (black) and fluorescence (dark red) spectra from 26 individual LH2 complexes. The bulk spectra were recorded at 4.5 K and those from the individual complexes at 1.2 K. The fluorescence excitation spectra in (b) are normalized with respect to the B850 peak intensity. The sum of single-complex emission spectra is scaled to the ensemble fluorescence spectrum according to the long-wavelength slope to better illustrate the emission missing from single-complex experiments. The two minima of the fluorescence anisotropy spectrum in (a) indicated by arrows have been shown to be associated with the edges of the B850 exciton state manifold [4,5,58]. See the text for further details.

The fluorescence excitation (blue), fluorescence (red), and fluorescence anisotropy (dark green) spectra of an ensemble of LH2 complexes are shown in Fig. 4. Drawn in parallel are the sums of single-complex excitation (black, the sum of 115 time-averaged spectra from 115 individual complexes) and fluorescence (dark red, the sum of 14 640 separate spectra from 26 individual complexes) spectra. As can be seen, peak positions of the B800 and B850 bands in the excitation spectra of the ensemble and single-complex samples coincide within the experimental uncertainty.

Despite this agreement, acknowledged also in [20], Fig. 4 shows a few clearly evident spectral differences. First, the fluorescence spectrum of the sum of single complexes is shifted toward longer wavelengths by a considerable amount, 6-7 nm, compared to the ensemble spectrum that peaks at 875 nm, which is also narrower. Second, the B850 band in the excitation spectrum of the sum of single complexes is much broader than it is in the respective ensemble spectrum. We note, in this regard, that the peak optical density of the samples was always <0.1, making the excitation spectra directly comparable to the absorption spectra calculated later.

What could cause these spectral differences? As analyzed in detail in [72], one practical problem arises from the necessity to use a fixed set of filters to block the scattered excitation laser light when finding the individual LH2 complexes and measuring the spectra. The bandpass filter set used for selecting individual complexes for measurement in [72] was transmitting light starting from 875 nm towards longer wavelengths. This is incidentally the maximum of the ensemble fluorescence signal. Hence, the complexes

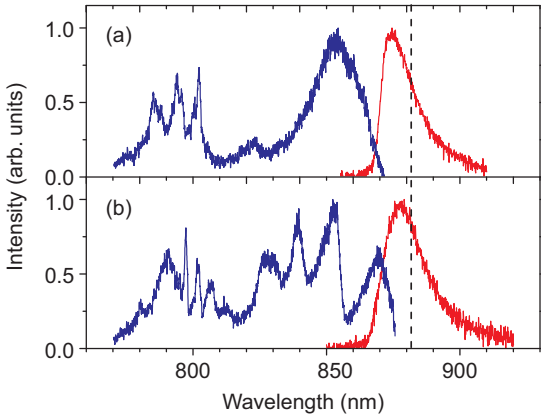

FIG. 5. (Color online) Examples of the time-averaged fluorescence excitation (blue) and time-averaged emission spectra (red) for two LH2 complexes that show radically different shapes of excitation spectra in the B850 range, one representing a smooth single band and the other a clear-cut multiband structure. The dashed vertical line designates the fluorescence spectrum peak position corresponding to the sum of all studied single complexes (14 640 separate exposures from 26 individual complexes as in Fig. 4).

fluorescing below 875 nm (in particular, those featuring a small Huang-Rhys factors) could not have been selectable for measurement. As a result, the experimental sampling might deviate from the statistical ensemble distribution, a likely reason for the observed differences between the two emission spectra in Fig. 4. It is also known that the complexes selected from the red edge of the absorption spectrum have a more developed STE character [6]. The respective complexes would be expected to emit more strongly and their spectra are not only more redshifted, but also broader. We will continue this discussion in Sec. IV, where we will present a more detailed modeling-based explanation for the discrepancies observed.

The qualitative similarity between the ensemble and the summed single-complex spectra observable in Fig. 4 is much more difficult to acknowledge when looking at the spectra of individual complexes. Presented in Fig. 5 are the time-averaged excitation and time-averaged fluorescence spectra for two individual LH2 complexes. The shapes of the spectra, averaged over 500 individual exposures of the same complex, differ quite drastically. Since the cumulative measurement period is long for both types of time-averaged spectra, it can be assumed that the complexes effectively cover a large part of the possible internal disorder realizations in case of both of them. The fluorescence excitation spectra of individual complexes feature remarkably more structure than might be expected from the uniform ensemble spectrum of Fig. 4. This simple example reveals the key advantage of single-molecule spectroscopy: Studies of individual complexes allow effective unmasking the ensemble-averaging effects of intra- and intercomplex disorders. As we have already remarked, the very large variations of the B850 absorption and excitation band structure in different complexes have previously been successfully replicated by introducing a disorder in the site energies with C_2 symmetry [12,57,75,76].

IV. DISCUSSION

A. Analysis of the single-complex fluorescence spectra

In this section we analyze the experimental data described in Sec. III using the theoretical model of Sec. II. In terms of the present model, the most important parameters of a single-complex fluorescence spectrum are the position of the ZPL and the Huang-Rhys factor, i.e., the excitation frequency E_0 of the lowest STE state and the respective Huang-Rhys factor S_0. To determine these from the experimental spectra, the line-shape model of Eq. (96) was fitted to the experimental single-complex spectra using a modified Levenberg-Marquardt [77] fitting algorithm. This method is preferred because it automatically takes into account the overlap between the PSB and ZPL (see Fig. 6). In fact, the present method does not require the ZPL to be clearly distinguishable in the experimental spectrum. Earlier, a simplified approach was used where a Gaussian or Lorentzian shaped ZPL was empirically fitted to the high-energy side of the PSB. This procedure can lead to serious overestimation of the ZPL intensity and to a corresponding decrease of the Huang-Rhys factor. In the case of the experiments described in [70], for example, the new method returns Huang-Rhys factors, which are by 0.4–0.6 larger than the values estimated in the original work.

Spectra from 26 individual LH2 complexes were available for the Huang-Rhys factor analysis. However, as high-noise spectra produce very large errors in the parameter determination (having little value but costing large amount of computing time) a preliminary selection of the complexes was made based on the signal-to-noise ratio. As a result, 17 complexes in total, amounting to about 8500 separate spectra (58% from 14 640), were selected for fitting.

Since the results of the fitting depend crucially on the starting parameters, the Levenberg-Marquardt algorithm was

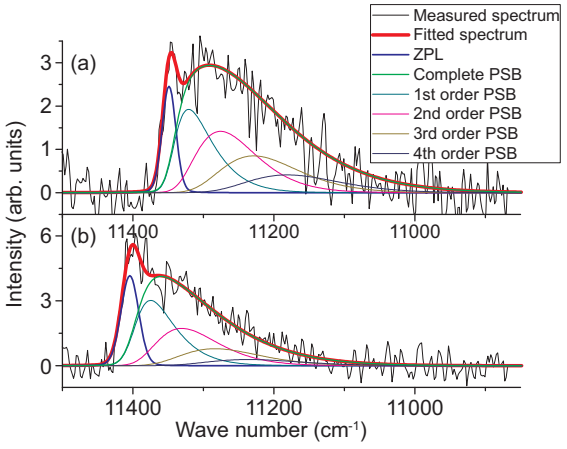

FIG. 6. (Color online) Two fluorescence spectra from the same LH2 complex, recorded at 1.2 K within 5 s with a spectral resolution of 7 cm^{-1}. The modeled line shapes, fitted to the noisy experimental spectra, are shown by bold red lines. The modeled shapes are considered to be the line shapes of STE corresponding to the $k = 0$ state, as per Eq. (9). Thin colored lines represent different ZPL and PSB components within the modeled spectra, as explained in (a). The separate components are shown for illustrative purposes; in fact, the bold red spectra were directly calculated and they effectively include an infinite number of components. See the text for details.

used twice. In the first stage a set of coarse-grained initial parameters was obtained to be applied as an input to the second, more precise, fitting step, which produced realistic line shapes suitable for analysis. To ensure that the fitting was not biased, we compared the full width at half maximum (FWHM) of all the spectra to the FWHMs of successfully fitted spectra and found no systematic differences. Slight fluctuations of disorder, producing small shifts of ZPLs within the spectral resolution, would, if present, lead to simple broadening of ZPL, which was also taken into account as a fitting parameter. Large fluctuations, on the other hand, may cause multiple ZPL-like peaks to appear in the spectrum. These latter cases were automatically eliminated from the analysis because they caused the algorithm to converge into a poor fit. Approximately 5000 spectra out of 8500 spectra chosen for analysis (or ∼59%) returned good fits, based on a weighted least-squares cost function. Figure 6 demonstrates two examples of such successful fits.

In Fig. 7 the Huang-Rhys factors S_0 obtained from the fitting are plotted as a function of the corresponding ZPL positions E_0. The close to 5000 points of this figure correspond to fitting of 5000 individual fluorescence spectra from 17 LH2 complexes. The characteristic frequency ω_c [see Eq. (5)] was fixed at 24 cm^{-1} in these fits, as the theoretical model only takes variations of the Huang-Rhys factor into account. This specific value of ω_c was found as a median from the coarse-grained fits to the data set with ω_c as the free parameter. The same ω_c value was used in all subsequent models.

The data points in Fig. 7 representing individual LH2 complexes have a tendency to cloud together, justifying the introduction of two separate forms of disorder: intracomplex and intercomplex. Figure 7(a) shows the correlation between the Huang-Rhys factor and the ZPL position. Following closely the Huang-Rhys factor distributions for particular complexes, as shown in the inset of Fig. 7(a), it can be noticed that the more redshifted spectra have generally higher S-factors. This trend agrees well with the previous results obtained from both the bulk difference fluorescence line-narrowing [78–80] and single-complex [19,70–72] measurements.

In Fig. 7(a) large numbers of spectra were discarded, requiring verification that the specific selection did not produce any bias. To account for all the recorded single spectra, they were convoluted with a Gaussian distribution of 110 cm^{-1} FWHM. This procedure smoothed out ZPLs in all the spectra, allowing for a more stable determination of the position and width of the spectra. The dependence of the FWHM for the 14 640 individual spectra on their spectral position is plotted in Fig. 7(b). Different colors and symbols [same as in Fig. 7(a)] signify individual complexes. As the tendencies in Figs. 7(a) and 7(b) appear qualitatively similar, we consider the data in Fig. 7(a) adequate. This conclusion will be verified later also by theoretical modeling.

While we just established a general increase of the Huang-Rhys factor or FWHM with the spectral redshift of the ZPL for the spectra of a single complex, such a correlation between different complexes is apparently missing. According to bulk ensemble data, the complexes with a median ZPL toward lower frequencies are expected to have higher median Huang-Rhys factors. We will present a possible explanation for this contradictorily observation in Sec. IV C.

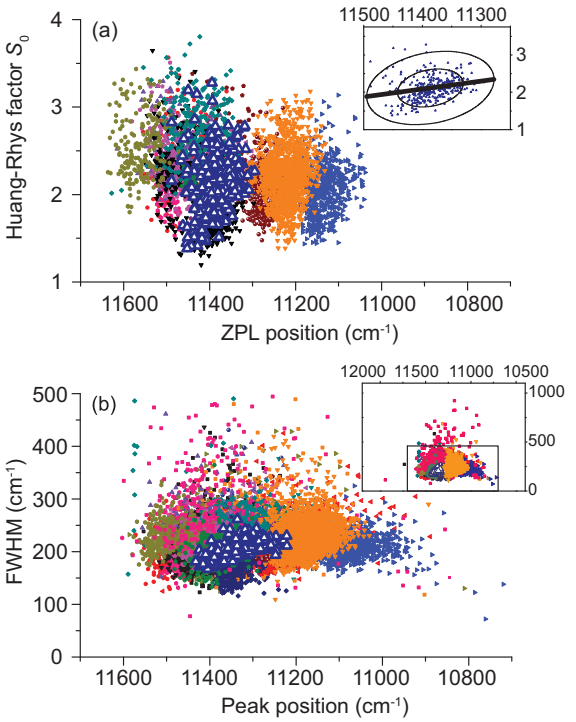

FIG. 7. (Color online) (a) Correlation between the Huang-Rhys factor and the ZPL frequency in the set of about 5000 fluorescence spectra from 17 selected LH2 complexes. Different colors and symbols signify data from different measured complexes, while each symbol represents a single spectrum. The spectra from one selected complex are marked with enlarged open triangles. Data for the same complex are provided in the inset along with the 99% and 95% confidence ellipses and the linear regression fit to highlight the dependence. (b) Dependence between the FWHMs and the peak frequencies of the smoothed single-complex fluorescence spectra corresponding to more than 99.5% of all the experimental spectra. Full extent of data points can be seen in the inset, which includes 14 631 data points (for 9 points the FWHM was not determinable). The same symbols and colors were used for the overlapping complexes in (a) and (b). The x axis runs from high to low energy to maintain correlation with the experimental spectra presented in wavelength scale. See the text for further explanation.

B. Modeling of the bulk ensemble spectra

Our aim here is to simultaneously model the single-complex and the ensemble spectra. This task is problematic from the outset since, as noted earlier, the sums of single-complex excitation and fluorescence spectra differ from the ensemble spectra. One simple reason for this incompatibility might be that the ensemble (Fig. 4) and single-complex spectra (Figs. 5 and 6) were not measured from exactly one and the same sample preparation and certainly not at the same time. Variations of the absorption and fluorescence spectral positions of up to 2 nm between different measurements is rather common for the samples considered here [20], which have previously raised serious concerns in data fitting [81,82]. Assuming that ensemble spectra are by default unbiased, we fitted the model to the ensemble data first, simultaneously taking care that the model would also fit the properties of single-complex spectra (Fig. 7) as well as possible.

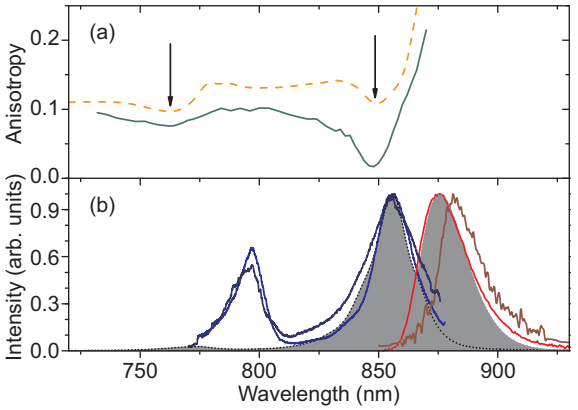

FIG. 8. (Color online) Comparison of the experimental LH2 spectra (solid lines, the same as in Fig. 4) with the modeled ensemble spectra of the B850 chromophore rings (filled area spectra and the dashed anisotropy spectrum). Calculations were performed over 5000 realizations of the inter- and intracomplex disorder. The B850 absorption, excitation and fluorescence spectra are normalized to 1.

The modeled B850 bulk ensemble spectra are shown in Fig. 8, along with the experimental spectra from the LH2 complexes. As can be seen in Fig. 8(b), the absorption and fluorescence excitation and fluorescence spectra overlap reasonably, although there are some characteristic differences in the shape. Spectral minima in the simulated and modeled fluorescence excitation anisotropy spectra [Fig. 8(a)] also agree reasonably well with each other, while the absolute value of the anisotropy is not that well reproduced. This discrepancy could come from different sources. First and foremost, we did not optimize angular placement of the transition dipole moments in this work, as we did previously [4], because of the already high number of free fitting parameters. This influences both the background level of the calculated anisotropy and the depth of the anisotropy minima. Although structural models of the LH2 complex from *Rps. acidophila* exist [21,40], they are not precise enough to model optical spectra without any adjustments in atomic positions and molecular orientations. Another reason could be the simplified line-shape model used, which could contribute to the mismatch in the redmost edge of the fluorescence spectrum. Also, according to our experience, the experimental anisotropy background is very sensitive to the quality of the sample, slightly varying from measurement to measurement.

Table I contains the best-fit parameters retrieved from the calculations. These parameters are not directly comparable with the parameters recovered in [4] because the disorder and self-trapping models used differ from each other. Earlier [4], the absorbing states were modeled as Frenkel excitons [26] described by the disordered rigid-lattice Hamiltonian and the emitting states as exciton polarons or STEs described by the Su-Schrieffer-Heeger (SSH) Hamiltonian [29]. Here, both the emitting and absorbing STE states were calculated according to the same SSH Hamiltonian. The other main difference arises from a more detailed disorder model that explicitly distinguishes between the intracomplex and the intercomplex disorder.

The most salient finding in Table I is the very large value of the site Huang-Rhys factor S when compared with the experimentally evaluated S factors for monomeric BChl *a* molecules not only in normal solvents [83], but also in proteins, such as Fenna-Matthews-Olson complex [84]. Although relevant, this is not a new result, being noticed in [7,58,85] and rather thoroughly discussed in [6,85,86]. The large-S factor, reflecting strong electron-phonon coupling, can in the tightly assembled B850 ring be explained by the involvement of charge transfer states [62]. The presence of charge transfer states in bacterial light-harvesting complexes is supported both by the experimental observations of electrochromic (Stark) effect [87,88] and very large pressure-induced spectral band shifts [89] and by the theoretical quantum chemical calculations [48,90–92].

C. Valuation of the single-complex spectra

Armed with the model parametrized in Sec. IV B, we now attempt to reproduce the experimental data of Figs. 5 and 7 theoretically. We start with producing analogs for the strongly fluctuating single-complex excitation and fluorescence spectra shown in Fig. 5. Figure 9 demonstrates spectral shapes for the four simulated complexes with rather different average Huang-Rhys factors, involving STE-like [Fig. 9(a)] and excitonlike

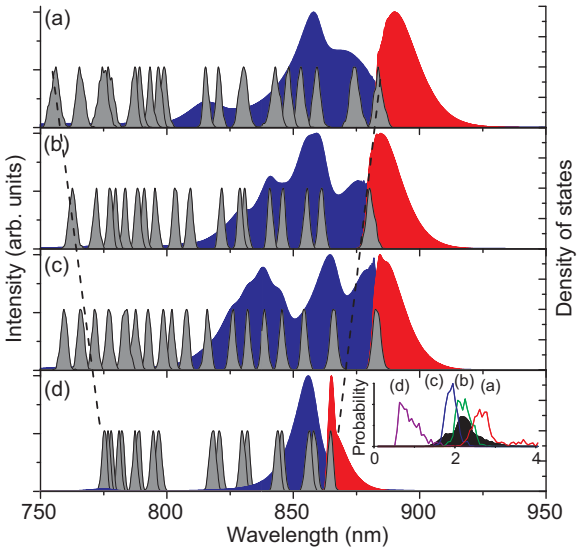

FIG. 9. (Color online) Simulated absorption (blue) and fluorescence (red) spectra of the B850 complex. The spectra are averaged over 500 intracomplex disorder realizations and modeled by applying the same spectral resolution as used in single-complex measurements shown in Fig. 5. Different panels show the spectra for different realizations of intercomplex disorder, selected from a simulated set of complexes by their Huang-Rhys factors with decreasing order from (a) to (d). Eighteen gray lines in each spectrum denote the densities of individual exciton states. Dashed lines through the highest- and lowest-energy exciton states indicate the general tendency of exciton band broadening with increasing Huang-Rhys factor. The inset shows the area-normalized histograms of S_0 for the complexes at fixed intercomplex disorder and at variant intracomplex disorder on the backdrop of the Huang-Rhys factors from experimental spectra [black, the same as in Fig. 10(b)].

[Fig. 9(d)] spectra as limiting cases represented by small and large Huang-Rhys factors, respectively. The spectra are averaged over the 500 intracomplex disorder realizations, as required for comparison with the experimental spectra of single complexes recorded over a long measurement time.

It can be seen from Fig. 9 that the distribution of the exciton states could vary between the complexes greatly, causing large differences in the structure of the absorption spectrum. This figure illustrates and clarifies several of the earlier observations, some of them also in passing discussed above, such as (i) the fluorescence spectra of excitonlike complexes are generally narrower than the exciton polaronlike spectra, (ii) only the excitonlike spectra reveal a narrow $k = 0$ ZPL at the origin of the absorption or fluorescence spectra, (iii) the fluorescence spectra tend to redshift, (iv) the absorption spectra tend to blueshift and broaden in correlation with increasing exciton-phonon coupling, and (v) as a direct consequence of (iii) and (iv), the Stokes shift between the absorption and fluorescence spectra increases with the exciton-phonon coupling. It has to be admitted that in the experiment this clear dependence between the structure of the excitation and fluorescence spectra was not observed. This might be due to the smaller range of complexes detected in the experiment, as will be explained below.

It can also be observed from Fig. 9 that the exciton state manifold (exciton zone in solid state physics parlance) widens upon increasing the exciton-phonon coupling. The two inclined dashed lines approximately drawn through the $k = 0$ state at the bottom of the exciton zone and the $k = 17$ state at its top illustrate this trend. This is counterintuitive because wider exciton zone would normally indicate stronger exciton interactions related to more delocalized exciton, while stronger exciton-phonon coupling would result in narrower zone with the more localized exciton. Analysis shows that in disordered systems, self-trapping of the exciton may actually promote exciton interactions in small parts of the system, effectively forming energetically differing subzones. This in turn may result in apparent widening of the zone [93]. More research into this interesting phenomenon is needed.

The data reproducing distributions in Fig. 7 are shown in Fig. 10, where Figs. 10(a) and 10(b) relate to the Huang-Rhys factor dependences and Figs. 10(c) and 10(d) to FWHM dependences in the smoothed spectra. The same smoothing procedure as in Fig. 7(b) was applied.

It can be seen from Fig. 10(a) that our model predicts a clear increase of the Huang-Rhys factors for the $k = 0$ state (S_0) along with lowering the state energy (E_0, experimentally available as the ZPL position), similar to the behavior of individual spectra for the LH2 complexes in Fig. 7. Curiously, almost all the experimentally measured complexes fall into a narrow slice of the theoretically available trace at around $S_0 \approx 2$. This might explain the apparently contradictorily

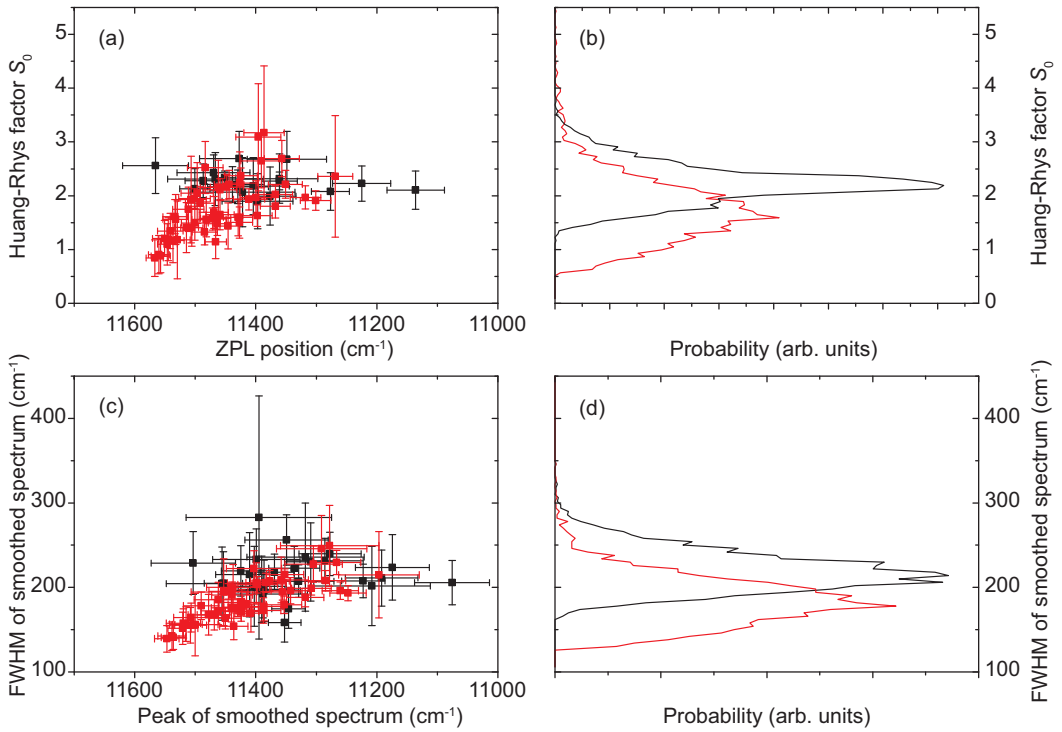

FIG. 10. (Color online) (a) Correlation between the Huang-Rhys factors S_0 and the ZPL frequency E_0 in the modeled (red) and experimental (black) fluorescence spectra of B850 complexes. Data corresponding to 50 modeled and a subset of 17 measured single complexes are shown. Five hundred intracomplex disorder realizations were applied in the modeling for each complex. (b) Histogram of the corresponding Huang-Rhys factors for the sum of all complexes. (c) and (d) Equivalent FWHM versus peak position plots for the smoothed spectra for all the measured complexes (total 26). The solid squares in (a) and (c) indicate the median of the corresponding values over the realizations of intracomplex disorder and error bars, the first and third quartiles. The modeled histograms in (b) and (d) were calculated form 5000 realizations of intra- and intercomplex disorder. The axes in (a) and (c) are running from high to low energy to be comparable with the experimental data that are in the wavelength scale.

observation from Fig. 7 that while within each and every complex there was a clear increase of S_0 with a decrease of the $k = 0$ state energy, no such trend was seen between different complexes. The experimental spectra also systematically tend to have larger variation in the ZPL positions and Huang-Rhys factors than predicted by the current model.

In Fig. 10(b) the theoretical model predicts an extended S_0 distribution that spans from about 0.5 (equivalent to very weakly coupled excitons) to 3–4 (very strongly coupled exciton polarons or STEs) along the long tail of the distribution. The distribution peaks at $S_0 \approx 1.6$. This behavior is in very good agreement with the selective spectroscopy data performed on ensembles of LH2 complexes [7,94,95]. The experimentally measured distribution of single complexes and the modeled distributions overlap, but complexes with lower Huang-Rhys factors corresponding to higher ZPL energies are clearly underrepresented in the experimental data set.

The smoothed spectral data presented in Figs. 10(c) and 10(d) verify the above behaviors in a more robust way. The fact that the model agrees with the experiment in the case of both the fitted line-shape data (which was only possible for a subset of complexes) and the smoothed spectral data of the whole data set serves as a proof that there is no systematic conflict between these two representations.

The reason for the general redshift of the fluorescence spectra observed in Figs. 10(a) and 10(c) with increasing electron-phonon coupling requires more research to be thoroughly explained. Qualitatively, however, the situation is as follows. The $k = 0$ state exciton self-traps into the lowest possible energetic state promoted by the disorder in the system [6,96,97]. Greater disorder favors more localized excited states with lower energy. Since, as noted in Sec. II, the Huang-Rhys factor is proportional to the participation ratio (the inverse of the delocalization length), the observed correlation between the redshift of the emission and the Huang-Rhys factor is anticipated.

Finally, we briefly comment on the correlation between the ZPL energy and the square of the transition dipole moment (relative dipole strength of emission) for the $k = 0$ exciton state of single complexes, using the same model ensemble as in Fig. 10. It can be seen from Fig. 11(a) that the dipole strength for the most excitonlike excitations (on the blue side of the spectrum) is rather weak. Dipole strength rapidly increases towards longer wavelength, leveling off at $\sim$11400 cm^{-1} ($\approx$877 nm). Upon a further redshift, the intensity starts to decline slightly. Similar behavior of exciton polarons was previously demonstrated and analyzed in [6,86,93]. Figure 11(b) compares the experimental and model distributions of finding the B850 ring systems at particular ZPL positions, with the result that the experimental distribution clearly overestimates the amount of the strongly redshifted spectra.

Figures 9 and 10 together give a plausible explanation for the observed discrepancy between the ensemble spectra and the sums of single spectra, first mentioned in connection with Fig. 4. Provided the selection of measured complexes predominantly contains complexes with a larger-S factor, the sum of the corresponding excitation spectra would be wider and the emission spectrum would be more redshifted than in the case of the full ensemble. This also means that the set of single-complex spectra analyzed in this work has been biased toward larger S as well as a broader FWHM. Taking into account the cutoff characteristics of the filter (bandpass from 875 to 925 nm, i.e., 11 430 to 10810 cm^{-1}) used when selecting complexes for measurement, it is becomes very clear why there are very few spectra with ZPL energies above 11450 cm^{-1}. The complexes with characteristics similar to the one shown in Fig. 9(d) simply lie outside the detection range of the system, leaving only more STE-like complexes for observation.

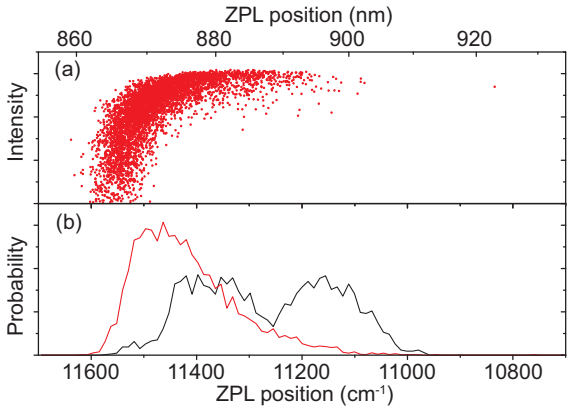

FIG. 11. (Color online) (a) Dependence of the modeled relative dipole strength of emission on the ZPL position (5000 realizations of inter- and intracomplex disorders). (b) Histograms of the ZPL positions (density of the $k = 0$ states) in the model ensemble of frame (a) (red) and the analyzed experimental data set (black).

V. CONCLUSION

In this work the previously obtained low-temperature optical spectra of individual LH2 photosynthetic antenna complexes [70–72], as well as their ensemble counterparts [20], were analyzed simultaneously. A phenomenological theoretical model, which combines strong exciton-phonon coupling with significant quasistatic disorder, was developed based on this analysis. The disorder model distinguishes between intracomplex and intercomplex disorders due, respectively, to slow conformational dynamics of proteins and static but spatially varying environment. This model is able to reproduce both static spectral differences detected between separate complexes and the slow temporal variations of the spectra of individual complexes not only qualitatively, but also quantitatively. The experimentally observed dependences of the Huang-Rhys factors, spectral widths, and dipole moments on the energetic position of the ZPL could also be satisfactorily reproduced. Model evaluations strongly suggest that the LH2 single-complex measurements performed thus far likely misrepresent the statistical ensemble revealed by bulk measurements. This may at least partly explain the existing differences between the single-complex and bulk spectroscopic data. The insight produced by this analysis would not have been available based on either ensemble or single-complex spectroscopy alone: Single-complex spectroscopy provided the means to directly observe the intracomplex disorder, while the range of extra-complex disorder would have been misjudged by the single-complex spectra alone. This work consequently

emphasizes the importance of the unified analysis of ensemble and single-complex optical spectral data.

ACKNOWLEDGMENTS

The Estonian Research Council Grant No. 13028I and the graduate school Functional Materials and Technologies, receiving funding from the European Social Fund under Project No. 1.2.0401.09-0079 in Estonia, supported this work. R.K. and J.K. acknowledge financial support from the Deutsche Forschungsgemeinschaft (Grants No. KO 1359/16-1, No. GZ: 436 EST 113/4/0-1, and No. GRK1640) and the State of Bavaria within the initiative Solar Technologies go Hybrid.

[1] R. J. Cogdell, A. Gall, and J. Köhler, Quart. Rev. Biophys. **39**, 227 (2006).
[2] H. Van Amerongen, L. Valkunas, and R. Van Grondelle, in *Photosynthetic Excitons* (World Scientific, Singapore, 2000), p. 590.
[3] G. D. Scholes and G. Rumbles, Nat. Mater. **5**, 683 (2006).
[4] M. Pajusalu, M. Rätsep, G. Trinkunas, and A. Freiberg, Chem. Phys. Chem. **12**, 634 (2011).
[5] A. Freiberg, M. Pajusalu, and M. Rätsep, J. Phys. Chem. B **117**, 11007 (2013).
[6] A. Freiberg and G. Trinkunas, in *Photosynthesis in Silico. Understanding Complexity From Molecules to Ecosystems*, edited by A. Laisk, L. Nedbal, and Govindjee (Springer, Heidelberg, 2009), p. 55.
[7] A. Freiberg, M. Rätsep, K. Timpmann, G. Trinkunas, and N. W. Woodbury, J. Phys. Chem. B **107**, 11510 (2003).
[8] K. Timpmann, Z. Katiliene, N. W. Woodbury, and A. Freiberg, J. Phys. Chem. B **105**, 12223 (2001).
[9] M. A. Bopp, Y. Jia, L. Li, R. J. Cogdell, and R. M. Hochstrasser, Proc. Natl. Acad. Sci. USA **94**, 10630 (1997).
[10] A. M. van Oijen, M. Ketelaars, J. Köhler, T. J. Aartsma, and J. Schmidt, J. Phys. Chem. B **102**, 9363 (1998).
[11] C. Tietz, O. Chekhlov, A. Dräbenstedt, J. Schuster, and J. Wrachtrup, J. Phys. Chem. B **103**, 6328 (1999).
[12] S. Tubasum, R. Camacho, M. Meyer, D. Yadav, R. J. Cogdell, T. Pullerits, and I. G. Scheblykin, Phys. Chem. Chem. Phys. **15**, 19862 (2013).
[13] M. Brecht, Mol. Phys. **107**, 1955 (2009).
[14] M. Brecht, S. Skandary, J. Hellmich, C. Glöckner, A. Konrad, M. Hussels, A. J. Meixner, A. Zouni, and E. Schlodder, Biochim. Biophys. Acta Bioenerg. **1837**, 773 (2014).
[15] K. Leiger, L. Reisberg, and A. Freiberg, J. Phys. Chem. B **117**, 9315 (2013).
[16] D. Rutkauskas, V. Novoderezkhin, R. J. Cogdell, and R. van Grondelle, Biochemistry **43**, 4431 (2004).
[17] A. M. van Oijen, M. Ketelaars, J. Köhler, T. J. Aartsma, and J. Schmidt, Science **285**, 400 (1999).
[18] R. J. Cogdell and J. Köhler, Biochem. J. **422**, 193 (2009).
[19] M. Hussels and M. Brecht, Biochemistry **50**, 3628 (2011).
[20] R. Kunz, K. Timpmann, J. Southall, R. J. Cogdell, J. Köhler, and A. Freiberg, J. Phys. Chem. B **117**, 12020 (2013).
[21] G. McDermott, S. M. Prince, A. A. Freer, A. M. Hawthornthwaite-Lawless, M. Z. Papiz, R. J. Cogdell, and N. W. Isaacs, Nature (London) **374**, 517 (1995).
[22] V. Cherezov, J. Clogston, M. Z. Papiz, and M. Caffrey, J. Mol. Biol. **357**, 1605 (2006).
[23] J. Moreland, A. Gramada, O. Buzko, Q. Zhang, and P. Bourne, BMC Bioinf. **6**, 21 (2005).
[24] D. Xu and Y. Zhang, PLoS ONE **4**, e8140 (2009).
[25] H. M. Wu, S. Savikhin, N. R. S. Reddy, R. Jankowiak, R. J. Cogdell, W. S. Struve, and G. J. Small, J. Phys. Chem. **100**, 12022 (1996).
[26] J. Frenkel, Phys. Rev. **37**, 1276 (1931).
[27] H. Fidder, J. Knoester, and D. A. Wiersma, J. Chem. Phys. **95**, 7880 (1991).
[28] T. Holstein, Ann. Phys. (N.Y.) **8**, 325 (1959).
[29] A. J. Heeger, S. Kivelson, J. R. Schrieffer, and W.-P. Su, Rev. Mod. Phys. **60**, 781 (1988).
[30] M. Marcus, O. R. Tozer, and W. Barford, J. Chem. Phys. **141**, 164102 (2014).
[31] J. Ye, K. Sun, Y. Zhao, Y. Yu, C. K. Lee, and J. Cao, J. Chem. Phys. **136**, 245104 (2012).
[32] A. H. Romero, D. W. Brown, and K. Lindenberg, Phys. Rev. B **60**, 4618 (1999).
[33] G. Venzl and S. F. Fischer, Phys. Rev. B **32**, 6437 (1985).
[34] L. Wang, D. Beljonne, L. Chen, and Q. Shi, J. Chem. Phys. **134**, 244116 (2011).
[35] A. Troisi and G. Orlandi, Phys. Rev. Lett. **96**, 086601 (2006).
[36] A. Troisi, D. L. Cheung, and D. Andrienko, Phys. Rev. Lett. **102**, 116602 (2009).
[37] A. Troisi, J. Chem. Phys. **134**, 034702 (2011).
[38] W. Barford and M. Marcus, J. Chem. Phys. **141**, 164101 (2014).
[39] K. Noba and Y. Kayanuma, J. Phys. Soc. Jpn. **67**, 3972 (1998).
[40] M. Z. Papiz, S. M. Prince, T. Howard, R. J. Cogdell, and N. W. Isaacs, J. Mol. Biol. **326**, 1523 (2003).
[41] J. Neugebauer, J. Phys. Chem. B **112**, 2207 (2008).
[42] M. H. C. Koolhaas, R. N. Frese, G. J. S. Fowler, T. S. Bibby, S. Georgakopoulou, G. van der Zwan, C. N. Hunter, and R. van Grondelle, Biochem. **37**, 4693 (1998).
[43] G. D. Scholes and G. R. Fleming, J. Phys. Chem. B **104**, 1854 (2000).
[44] C. Hofmann, T. J. Aartsma, and J. Köhler, Chem. Phys. Lett. **395**, 373 (2004).
[45] S. Jang and R. J. Silbey, J. Chem. Phys. **118**, 9324 (2003).
[46] B. P. Krueger, G. D. Scholes, and G. R. Fleming, J. Phys. Chem. B **102**, 5378 (1998).
[47] A. Damjanovic, I. Kosztin, U. Kleinekathöfer, and K. Schulten, Phys. Rev. E **65**, 031919 (2002).
[48] J. Linnanto, A. Freiberg, and J. Korppi-Tommola, J. Phys. Chem. B **115**, 5536 (2011).
[49] A. Freiberg, K. Timpmann, R. Ruus, and N. W. Woodbury, J. Phys. Chem. B **103**, 10032 (1999).
[50] A. M. van Oijen, M. Ketelaars, J. Köhler, T. J. Aartsma, and J. Schmidt, Biophys. J. **78**, 1570 (2000).
[51] R. Agarwal, A. H. Rizvi, B. S. Prall, J. D. Olsen, C. N. Hunter, and G. R. Fleming, J. Phys. Chem. A **106**, 7573 (2002).
[52] C. Hofmann, T. J. Aartsma, H. Michel, and J. Köhler, Proc. Natl. Acad. Sci. USA **100**, 15534 (2003).

[53] C. Hofmann, T. J. Aartsma, H. Michel, and J. Köhler, New J. Phys. **6**, 8 (2004).
[54] J. Baier, M. F. Richter, R. J. Cogdell, S. Oellerich, and J. Köhler, Phys. Rev. Lett. **100**, 018108 (2008).
[55] S. Tubasum, R. J. Cogdell, I. G. Scheblykin, and T. Pullerits, J. Phys. Chem. B **115**, 4963 (2011).
[56] U. Gerken, F. Jelezko, B. Götze, M. Branschädel, C. Tietz, R. Ghosh, and J. Wrachtrup, J. Phys. Chem. B **107**, 338 (2002).
[57] S. Jang, R. J. Silbey, R. Kunz, C. Hofmann, and J. Köhler, J. Phys. Chem. B **115**, 12947 (2011).
[58] K. Timpmann, G. Trinkunas, J. D. Olsen, C. N. Hunter, and A. Freiberg, Chem. Phys. Lett. **398**, 384 (2004).
[59] K. Timpmann, G. Trinkunas, P. Qian, C. N. Hunter, and A. Freiberg, Chem. Phys. Lett. **414**, 359 (2005).
[60] A. Freiberg, K. Timpmann, and G. Trinkunas, Chem. Phys. Lett. **500**, 111 (2010).
[61] S. Jang, J. Cao, and R. J. Silbey, J. Phys. Chem. B **106**, 8313 (2002).
[62] M. Rätsep, M. Pajusalu, J. M. Linnanto, and A. Freiberg, J. Chem. Phys. **141**, 155102 (2014).
[63] M. Pajusalu, M. Rätsep, and A. Freiberg, J. Lumin. **152**, 79 (2014).
[64] J. M. Hayes, J. K. Gillie, D. Tang, and G. J. Small, Biochim. Biophys. Acta Bioenerg. **932**, 287 (1988).
[65] M. Lax, J. Chem. Phys. **20**, 1752 (1952).
[66] P. B. Walczak, A. Eisfeld, and J. S. Briggs, J. Chem. Phys. **128**, 044505 (2008).
[67] T. Renger and R. A. Marcus, J. Chem. Phys. **116**, 9997 (2002).
[68] K. Ohta, M. Yang, and G. R. Fleming, J. Chem. Phys. **115**, 7609 (2001).
[69] A. J. Leggett, S. Chakravarty, A. T. Dorsey, M. P. A. Fisher, A. Garg, and W. Zwerger, Rev. Mod. Phys. **59**, 1 (1987).
[70] R. Kunz, K. Timpmann, J. Southall, R. J. Cogdell, A. Freiberg, and J. Köhler, J. Phys. Chem. B **116**, 11017 (2012).
[71] R. Kunz, K. Timpmann, J. Southall, R. J. Cogdell, A. Freiberg, and J. Köhler, Angew. Chem. Int. Ed. Engl. **52**, 8726 (2013).
[72] R. Kunz, K. Timpmann, J. Southall, R. J. Cogdell, A. Freiberg, and J. Köhler, Biophys. J. **106**, 2008 (2014).
[73] M. F. Richter, J. Baier, R. J. Cogdell, J. Köhler, and S. Oellerich, Biophys. J. **93**, 183 (2007).
[74] P. S. Böhm, R. Kunz, J. Southall, R. J. Cogdell, and J. Köhler, J. Phys. Chem. B **117**, 3120 (2013).
[75] M. Ketelaars, A. M. van Oijen, M. Matsushita, J. Köhler, J. Schmidt, and T. J. Aartsma, Biophys. J. **80**, 1591 (2001).
[76] X. Hong, Y.-X. Weng, and M. Li, Biophys. J. **86**, 1082 (2004).
[77] K. Levenberg, Quart. Appl. Math. **2**, 164 (1944).
[78] M. Rätsep, M. Pajusalu, and A. Freiberg, Chem. Phys. Lett. **479**, 140 (2009).
[79] M. Rätsep, J. Pieper, K.-D. Irrgang, and A. Freiberg, J. Phys. Chem. B **112**, 110 (2008).
[80] A. Freiberg, M. Rätsep, K. Timpmann, and G. Trinkunas, Chem. Phys. **357**, 102 (2009).
[81] A. Kell, K. Acharya, R. E. Blankenship, and R. Jankowiak, Photosynth. Res. **120**, 323 (2014).
[82] X. Lu and R. M. Pearlstein, Photochem. Photobiol. **57**, 86 (1993).
[83] M. Rätsep, Z.-L. Cai, J. R. Reimers, and A. Freiberg, J. Chem. Phys. **134**, 024506 (2011).
[84] M. Rätsep and A. Freiberg, J. Lumin. **127**, 251 (2007).
[85] V. Urboniene, O. Vrublevskaja, G. Trinkunas, A. Gall, B. Robert, and L. Valkunas, Biophys. J. **93**, 2188 (2007).
[86] G. Trinkunas and A. Freiberg, J. Lumin. **119**, 105 (2006).
[87] L. M. P. Beekman, R. N. Frese, G. J. S. Fowler, R. Picorel, R. J. Cogdell, I. H. M. van Stokkum, C. N. Hunter, and R. van Grondelle, J. Phys. Chem. B **101**, 7293 (1997).
[88] M. Rätsep, H. M. Wu, J. M. Hayes, R. E. Blankenship, R. J. Cogdell, and G. J. Small, J. Phys. Chem. B **102**, 4035 (1998).
[89] K. Timpmann, A. Ellervee, T. Pullerits, R. Ruus, V. Sundström, and A. Freiberg, J. Phys. Chem. B **105**, 8436 (2001).
[90] R. G. Alden, E. Johnson, V. Nagarajan, W. W. Parson, C. J. Law, and R. G. Cogdell, J. Phys. Chem. B **101**, 4667 (1997).
[91] G. D. Scholes, I. R. Gould, R. J. Cogdell, and G. R. Fleming, J. Phys. Chem. B **103**, 2543 (1999).
[92] M. G. Cory, M. C. Zerner, X. Hu, and K. Schulten, J. Phys. Chem. B **102**, 7640 (1998).
[93] W. J. D. Beenken, M. Dahlbom, P. Kjellberg, and T. Pullerits, J. Chem. Phys. **117**, 5810 (2002).
[94] K. Timpmann, M. Rätsep, C. N. Hunter, and A. Freiberg, J. Phys. Chem. B **108**, 10581 (2004).
[95] A. Freiberg, M. Rätsep, K. Timpmann, and G. Trinkunas, J. Lumin. **108**, 107 (2004).
[96] D. Emin and T. Holstein, Phys. Rev. Lett. **36**, 323 (1976).
[97] G. Trinkunas and A. Freiberg, J. Lumin. **112**, 420 (2005).